# Numerical modeling of wheel-rail squeal-exciting contact

Yang, Zhen; Li, Zili

**DOI**
10.1016/j.ijmecsci.2019.02.012

**Publication date**
2019

**Document Version**
Final published version

**Published in**
International Journal of Mechanical Sciences

International Journal of Mechanical Sciences 153–154 (2019) 490–499

Contents lists available at ScienceDirect

International Journal of Mechanical Sciences

journal homepage: www.elsevier.com/locate/ijmecsci

# Numerical modeling of wheel-rail squeal-exciting contact

Zhen Yang, Zili Li*

*Delft University of Technology, Section of Railway Engineering, Stevinweg 1, 2628 CN Delft, The Netherlands*

ARTICLE INFO

*Keywords:*
Wheel-rail contact
Dynamic interaction
Squeal
Numerical modeling
Explicit FEM

ABSTRACT

Complex frictional rolling contact and high-frequency wheel dynamic behavior make modeling squeal greatly challenging. The falling-friction effect and wheel mode-coupling behavior are believed to be the two main mechanisms that generate unstable wheel vibration and the resulting squeal noise. To rigorously consider both mechanisms in one model, we propose an explicit finite element (FE) model to simulate wheel-rail dynamic frictional rolling. Wheel-rail squeal-exciting contact is investigated with considerations of dynamic effects, unsteady lateral creepage and velocity-dependent friction. With the inclusion of the dynamic effects in the contact solution, large-creepage-induced waves, which share features with Rayleigh waves, are discovered. The solutions of the dynamic contact calculated using the proposed model indicate that the explicit FE method is able to reproduce the falling-friction effect. The transient analyses of wheel-rail frictional rolling with wheel lateral creepage show the coupling of the axial and radial dynamics of the rolling wheel model, suggesting that the explicit FE method can also reproduce the mode-coupling behavior. This study improves the understanding and modeling of squeal-exciting contact from the perspective of wheel-rail dynamic interaction.

## 1. Introduction to friction-induced squeal

Squeal, which is an intrinsically nonlinear and transient phenomenon, poses great challenges in modeling [1]. Systematic studies on railway curve squeal began in the 1970s when Rudd [2] described the wheel-rail frictional characteristic (the functional dependence between friction force and wheel-rail relative velocity) in terms of 'negative damping' (generalized as full 'stick-slip') or 'falling friction', and associated this characteristic with the mechanism of wheel squeal. Since then, various increasingly sophisticated theoretical models have adopted parts of this mechanism based on Rudd's seminal model [3–8].

Analytical research [9], however, revealed that instability can also occur with constant or even positive creep force characteristics when additional mechanical degrees of freedom are considered. Similarly, finite element (FE) analyses by the complex eigenvalue approach revealed that instability arises when two modes couple in the presence of friction [10]. To consider the influence of the vertical dynamics on friction, the 'mode-coupling dynamic instability' mechanism have been employed in combination with falling-friction theories to predict friction-induced instability [8, 11–13]. Chiello, et al. [14] concluded that the two types of destabilization caused by the falling-friction mechanism and by the mode-coupling mechanism may be combined in each particular situation of squeal; thus, both mechanisms should be explored [15].

The generation of squeal is characterized as 'enigmatic' [16] or 'erratic' [17, 18] in railway research because field observations of squeal phenomena often fail to be explained by the existing theories. The contact modeling accounting for the frictional instability of a vibrating wheel is considered the central part of the squeal prediction model [19]. One shortcoming of the existing squeal prediction models is the incomplete representation of the contact model. The simplifications of the point contact models and Kalker's contact models with discretized contact surface (widely used in the existing squeal prediction models) have unknown influences on the prediction of friction-induced vibration [20]. As reported by a recent review of the squeal study [21], although Kalker's contact models can treat steady-state creepage, more detailed contact models that include transient effects may be needed for a correct representation of the squeal mechanisms.

This study proposes an explicit FE dynamic contact model to simulate wheel-rail squeal-exciting contact with unsteady lateral creepage. Unsteady lateral creepage, particularly between the leading inner wheel and the low rail, is thought to be the main cause of squeal [22]. The two commonly considered mechanisms leading to squeal—the falling-friction and mode-coupling mechanisms—are addressed in this study. In contrast with the steady-state contact assumed in Kalker's theories, the proposed explicit FE contact model accommodates the dynamic, or transient, effects involved in wheel-rail interactions by coupling the calculation of wheel-rail frictional rolling contact with the calculation of wheel/rail structural dynamics (see Section 2.1). Here, the dynamic effects denote that the inertia of material elements influences the stress field when the elements 'flow' through the deforming region [23]. With the inclusion of the dynamic effects in the contact solution, the

* Corresponding author.
*E-mail addresses:* z.yang-1@tudelft.nl (Z. Yang), z.li@tudelft.nl (Z. Li).

https://doi.org/10.1016/j.ijmecsci.2019.02.012
Received 5 November 2018; Received in revised form 14 January 2019; Accepted 11 February 2019
Available online 19 February 2019

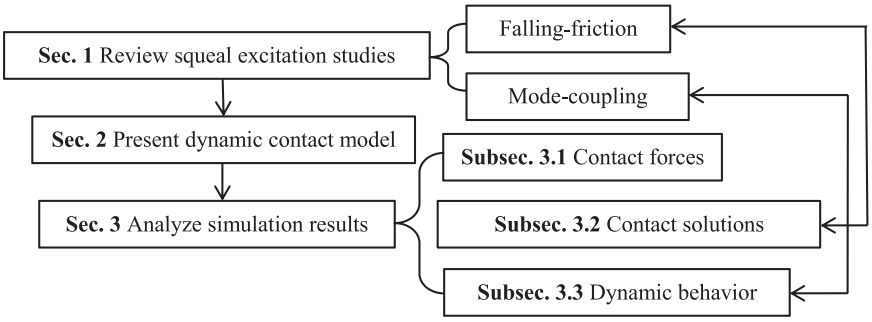


**Fig. 1.** The structure and the schematic logic of this study.

large-creepage-induced waves, which share features with Rayleigh waves, are discovered. This study refers to wheel-rail contact with structural dynamic effects as wheel-rail dynamic interaction. The aim of this work is to contribute to the better modeling and understanding of friction instability and squeal generation from the perspective of wheel-rail dynamic interaction.

Fig. 1 shows the structure and the schematic logic of this study. After reviewing studies on the two widely accepted generation mechanisms in Section 1, Section 2 presents the explicit FE wheel-rail dynamic interaction model. Section 3 then analyzes the simulated contact forces (Section 3.1), the dynamic contact solutions (Section 3.2) and the wheel dynamic behavior (Section 3.3). The analyses suggest that the explicit FE model can reproduce the falling-friction effect and the wheel mode-coupling behavior and thus confirm that the explicit finite element method (FEM) is suitable for modeling squeal-exciting contact.

## 2. Explicit FE wheel-rail dynamic interaction model

### 2.1. Algorithms of the explicit FE wheel-rail dynamic interaction analysis

This subsection summarizes the core algorithms employed in the explicit FE wheel-rail interaction analyses with a focus on the mathematical model and the numerical solution procedure. The explicit integration scheme uses the central difference method to approximate the acceleration vector ü. The equilibrium equation for the wheel-rail dynamic interaction problem at time step $t$ can be written as Eq. (1):

$$\ddot{\mathbf{u}}^t = \mathbf{M}^{-1}\left(\mathbf{f}_{\text{ext}}{}^t - \mathbf{f}_{\text{int}}{}^t + \mathbf{f}_{\text{con}}{}^t\right) \tag{1}$$

where $\mathbf{M}$, $\mathbf{f}_{\text{int}}$ and $\mathbf{f}_{\text{ext}}$ are the mass matrix, internal force vector and external force vector, respectively, and $\mathbf{f}_{\text{con}}$ is the contact force vector, which can be included as a contribution to the externally applied tractions [24,25]. The velocity and displacement vectors can then be obtained using central difference time integration via Eqs. (2) and (3):

$$\dot{\mathbf{u}}^{t+1/2} = \dot{\mathbf{u}}^{t-1/2} + \Delta t^{t+1/2}\ddot{\mathbf{u}}^t \tag{2}$$

$$\mathbf{u}^{t+1} = \mathbf{u}^t + \Delta t^{t+1}\dot{\mathbf{u}}^{t+1/2} \tag{3}$$

where $\Delta t$ is the time step size. The Courant–Friedrichs–Lewy stability condition [26] was used in this study to guarantee the convergence of the explicit integration, which requires that a sound wave may not cross the smallest element within one time step. The critical time step characterized by the smallest element may vary in nonlinear dynamic analysis [24] because of changes in the material parameters and/or geometry. A scale factor of 0.9 is thus employed to control the time step ($\Delta t = 0.9 \times$ critical time step), so that the convergence condition can be satisfied with certainty. In this study, the time step of the explicit integration $\Delta t \approx 86$ ns.

Table 1 outlines the numerical procedure for the explicit FE wheel-rail dynamic interaction analysis, which is composed primarily of calculations of the mass matrix and force vectors in equilibrium Eq. (1). A lumped mass matrix can be constructed prior to the iteration to promote

**Table 1**
Numerical procedure for the explicit FE wheel-rail dynamic interaction analysis.

| |
|---|
| Initialize algorithm: apply initial conditions; define contact pairs; construct the lumped mass matrix M; and set the termination time. |
| LOOP1 $t = 0, 1, 2, \ldots, n$ (time step number) |
| (I) Apply load conditions to construct the external force vector $\mathbf{f}^t_{\text{ext}}$. |
| (II) Process elements to construct the internal force vector $\mathbf{f}^t_{\text{int}}$. |
| (III) Construct the wheel-rail contact force vector $\mathbf{f}^t_{\text{con}}$ using the penalty contact method. |
| LOOP2 $N = 1, 2, \ldots, m$ (slave wheel node number) |
| i. Locate the master rail segment for the slave wheel node $N$. |
| ii. Locate the wheel-rail contact point (projection of the slave node on the master segment). |
| iii. Calculate the contact force. |
| END LOOP2 |
| (IV) Update the nodal accelerations $\ddot{\mathbf{u}}^t$, velocities $\dot{\mathbf{u}}^{t+1/2}$ and displacements $\mathbf{u}^{t+1}$. |
| (V) Check for termination. |
| END LOOP1 |
| Output: wheel/rail nodal force and nodal motion (ü, u̇ and u) |

the efficiency and practicality of the explicit FEM. For the force vectors, the external force vector $\mathbf{f}_{\text{ext}}$ can be calculated directly by the given load conditions; the internal force vector $\mathbf{f}_{\text{int}}$ contributed by stresses can be calculated by the constitutive and strain-displacement formulations built in the element and material models; and the contact force vector $\mathbf{f}_{\text{con}}$ can be calculated using the penalty contact method [27]. When the penalty contact algorithm is applied, the time step size $\Delta t$ used in the explicit integration should not exceed the contact-based critical time step to avoid contact instability. The contact-based critical time step determined by the penalty contact algorithm is proportional to $\min\{\sqrt{m^J/k}\}$ where $m^J$ ($J = 1,2$) is the mass attached to the contact "spring" and $k$ is the penalty contact stiffness [28]. In this study, the penalty contact-based critical time step is 118 ns, bigger than the time step of the explicit integration $\Delta t$ (86 ns); the convergence of contact calculation can, therefore, be guaranteed.

The numerical solution procedure presented in Table 1 contains two loops. The outer loop is constructed mainly by formulating the equation of motion and solving the equation with the central difference scheme. In contrast, the inner loop calculates the wheel-rail contact, which is called as a subroutine at each time step prior to updating the structural dynamic responses. The calculation of wheel/rail dynamics and the calculation of wheel-rail contact are therefore coupled in the numerical algorithm.

The Coulomb friction law is applied to solve the wheel-rail tangential contact [27]. A trial tangential contact nodal force $\mathbf{f}^*$ at time step $t+1$ can be defined as Eq. (4):

$$\mathbf{f}^* = \mathbf{f}_{\text{cT}}{}^t - k\Delta\mathbf{e} \tag{4}$$

where $\mathbf{f}_{\text{cT}}{}^t$ is the tangential contact force calculated at time step $t$, $k$ is the penalty contact stiffness, and $\Delta\mathbf{e}$ is the incremental movement of the slave wheel node along the rail surface. The traction bound $f_{\text{bound}}{}^t$ at time step $t$ in the Coulomb friction law is the product of the magnitude of the normal force $\mathbf{f}_{\text{cN}}{}^t$ at the same time step and the coefficient of friction

(COF) $\mu$, as Eq. (5):

$$f_{\text{bound}}{}^{t} = \mu\left|\mathbf{f}_{\text{cN}}{}^{t}\right| \tag{5}$$

The tangential contact force at time step $t+1$ can thus be written as Eq. (6):

$$\mathbf{f}_{\text{cT}}{}^{t+1} = \begin{cases} \mathbf{f}^{*} & if\ |\mathbf{f}^{*}| \le f_{\text{bound}}{}^{t+1} \\ f_{\text{bound}}{}^{t+1}\mathbf{f}^{*}/|\mathbf{f}^{*}| & if\ |\mathbf{f}^{*}| > f_{\text{bound}}{}^{t+1} \end{cases} \tag{6}$$

The COF $\mu$, which is considered a constant in the classical Coulomb's law, can vary with various factors in wheel-rail contact, such as sliding speed, contact pressure, surface lubrication or contamination, roughness, temperature and humidity [29]. Because the explicit FEM couples the calculation of wheel/rail dynamic responses with the calculation of wheel-rail contact in the time domain, a velocity-dependent Coulomb's law with a functional COF can be implemented in the explicit FEM. The COF updated at each time step can be expressed in terms of the static and dynamic friction coefficients $\mu_s$ and $\mu_d$, respectively, a decay constant $c$ and wheel-rail relative sliding velocities $\dot{\mathbf{u}}_{\text{rel}}$ between the slave nodes and master segments at the same time step using Eqs. (7) and (8):

$$\mu\left(\dot{\mathbf{u}}_{\text{rel}}\right) = \mu_d + \left(\mu_s - \mu_d\right)\mathrm{e}^{-c\left|\dot{\mathbf{u}}_{\text{rel}}\right|} \tag{7}$$

$$\dot{\mathbf{u}}_{\text{rel}=}\Delta\mathbf{e}/\Delta t \tag{8}$$

The decay constant $c$ describes how quickly the static coefficient approaches the dynamic coefficient and can be determined by fitting the measured results [29].

### 2.2. Wheel-rail dynamic interaction model with wheel lateral motion

Fig. 2(a) shows the employed three-dimensional explicit FE wheel-track dynamic interaction model with wheel lateral motion. A 10-m length of half-track and a half wheel set with sprung mass of the car body and the bogie were considered. The wheel, the rail and the sleepers were modeled using 8-node solid elements. To achieve high solution accuracy with a reasonable model size, nonuniform meshing was used. The mesh size around the initial position of the wheel-rail contact and

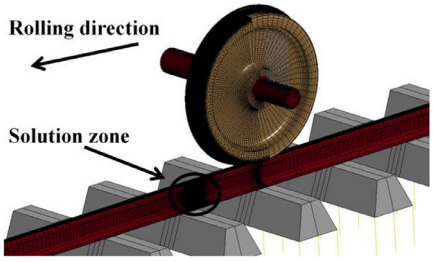


(a)

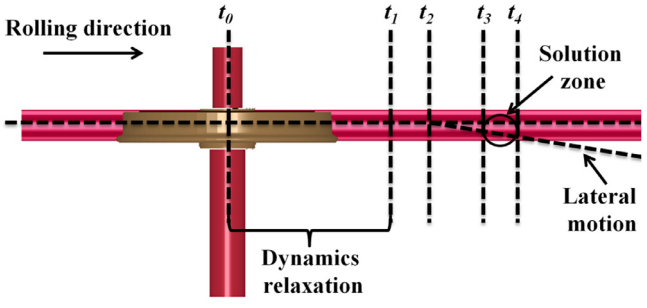


(b)

**Fig. 2.** Wheel-rail dynamic interaction model. (a) 3D FE model; (b) simulated frictional rolling with wheel lateral motion.

**Table 2**
Prescribed displacement boundary conditions applied to the simulation cases.

| Prescribed displacement boundary conditions | Simulation cases with a constant COF | Simulation case with a velocity-dependent COF |
|---|---|---|
| No lateral wheel motion | case 1 | |
| Small lateral wheel motion | case 2 | |
| Medium lateral wheel motion | case 3 | case 5 |
| Large lateral wheel motion | case 4 | |

the 150-mm length of the solution zone was 1 mm. The lumped mass of the car body and bogie was modeled as mass elements that were connected to the wheelset by the primary suspension of the vehicle with parallel linear springs and viscous dampers. Because the sleepers and ballast have little influence on the high-frequency dynamic behavior under study, each sleeper model contained only 12 solid elements and the ballast was simplified as vertical spring and damper elements with the displacement constrained in the lateral and longitudinal directions. The same constraint type was used at the two ends of the rail model. The parameters involved in the track model are taken primarily from [30]. The wheel-rail contact was defined with real geometry and with the wheel flange included. The wheel geometry corresponded to a passenger car wheel of the Dutch railway with the standard profile of S1002; the rail was UIC54E1 with an inclination of 1:40. No geometry irregularities were considered on the surfaces of the wheel or rail.

The wheel-rail dynamic interaction was simulated by employing the software ANSYS& LS-DYNA: the static equilibrium of the system under gravity was first solved with an implicit solver of ANSYS; and an explicit solver of LS-DYNA, whose core algorithms is presented in Section 2.1, was then employed to simulate wheel-rail dynamic frictional rolling. The dynamic simulation applied the displacement field calculated with the implicit solver for stress initialization. In the transient dynamic simulation, the wheel rolled from its initial position at time $t_0 = 0$ s to the solution zone with an initial speed of 100 km/h along the rail, as shown in Fig. 2(b). The dynamics arising from the wheel/rail initial kinematic and potential energy due to imperfect static equilibrium [31] have relaxed at time $t_1 = 15$ ms. The wheel lateral motion was subsequently simulated from time $t_2 = 16$ ms by applying the prescribed displacement boundary conditions listed in Table 2 to both ends of the wheel half-axle (except for in case 1). Note that, in this study, the angle of attack was approximated to zero because, in the simulations, the initial angles of attack were zero and both ends of the wheel half-axle model applied the same displacement boundary condition during transient rolling. Fig. 3(a) and (b) present the prescribed displacement boundary conditions applied in the simulations and the resulting lateral wheel displacements, respectively. The two graphs share the same trend, but the simulated displacements fluctuated due to the flexibility of the wheel and axle; the

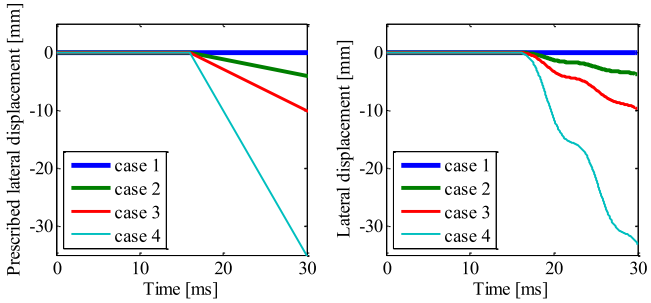


(a) (b)

**Fig. 3.** Time histories of the prescribed displacement boundary conditions and the resulting lateral wheel displacements. (a) Prescribed displacement boundary conditions applied to the simulation cases; (b) simulated resulting lateral wheel displacements.

unsteady lateral creepage was thus simulated. The wheel entered the solution zone at time $t_3 = 16.5$ ms and exited at $t_4 = 18.7$ ms. The dynamic evolution of the contact solutions was captured between $t_3$ and $t_4$.

A driving wheel was modeled in this study by applying a torque on the wheel axle. The torque initially increased gradually from zero until reaching its maximum value at 6 ms and remaining constant. A longitudinal creep force was thus generated. The explicit FEM can also be employed to simulate frictional rolling contact between a driven wheel and rail, e.g., by applying a longitudinal traction force on the wheel axle [32], which, however, produces a longitudinal creep force in the opposite direction. The corresponding traction coefficient equals the quotient of the longitudinal creep force and the wheel load and is considered to be constant in steady-state rolling [31], whereas it varies with time in dynamic rolling because of vibration. The quasi-steady-state traction coefficient was 0.27 in this study. A constant COF = 0.45 was used for simulation cases 1–4.

Knothe, et al. [33] reported that the falling-friction characteristic can be reproduced only by assuming that COF depends on the wheel-rail sliding velocity; simulation case 5 listed in Table 2 was therefore conducted with a velocity-dependent COF. Simulation case 5 shared the same configuration as case 3 (except for COF). When a velocity-dependent COF is applied, the overall COF may differ from the local COF at a node [29].

## 3. Analyses of wheel-rail contact and dynamics results

This section first analyzes the contact forces calculated by the explicit FE model in Section 3.1 to provide a broad overview of the wheel-rail dynamic interaction with wheel lateral motion. To reproduce the two potential mechanisms of squeal introduced in Section 1 (the falling-friction and mode-coupling mechanisms), the simulated wheel-rail dynamic contact solutions and structural dynamic responses are analyzed in Sections 3.2 and 3.3, respectively.

### 3.1. Contact forces

Fig. 4(a) and (b) show the time histories of the contact forces simulated without wheel lateral motion (case 1) and with medium lateral motion (case 3), respectively. Before time $t_1 = 15$ ms, the simulated contact forces fluctuated mostly due to vibrations excited by initial kinetic and potential energy in the unrelaxed system. The traction bound (denoted by the cyan curve) fluctuated around the static value 50 kN. It could be assumed that a quasi-steady state was entered after the oscillations were damped to less than 10% of the static values at time $t_1$. The creep force is the resultant force of the lateral and longitudinal contact forces. In Fig. 4(a), the simulated creep force (denoted by the red curve) almost overlaps the longitudinal force (denoted by the green curve) because the value of the lateral force (denoted by the blue curve) is small. By contrast, as shown in Fig. 4(b), the lateral force simulated by case 3 jumped to large value after $t_2 = 16$ ms due to the enforcement of a prescribed displacement boundary condition; consequently, the creep force reached the traction bound and friction saturation occurred at approximately 19 ms. The dynamic evolution of the contact solution between times $t_3 = 16.5$ ms and $t_4 = 18.7$ ms were output and are analyzed in the next subsection.

### 3.2. Contact solutions

This subsection analyzes the dynamic contact solutions calculated using the proposed explicit FE wheel-rail interaction model, including contact stresses and the distributions of micro-slip and adhesion-slip regions within the contact patch. This subsection also discusses the influences of lateral creepage and velocity-dependent COF on the dynamic contact solutions.

#### 3.2.1. Contact solutions with dynamic effects

Fig. 5(a) shows a magnified view of the time histories of the contact forces calculated by case 1 between times $t_3 = 16.5$ and $t_4 = 18.7$ ms (within the solution zone). The close-up view shows that the simulated traction bound and creep force oscillated periodically but were not exactly in phase. Eight time points with a fixed interval (0.06 ms) were selected from a certain period of the creep force fluctuation, designated 1–8 in the magnified view in Fig. 5(a). Fig. 5(b) plots the distributions of the simulated surface shear stress (red curve) and traction bound (blue curve) within the contact patch at these eight selected time points. The adhesion and slip regions determined by the contact stress are denoted

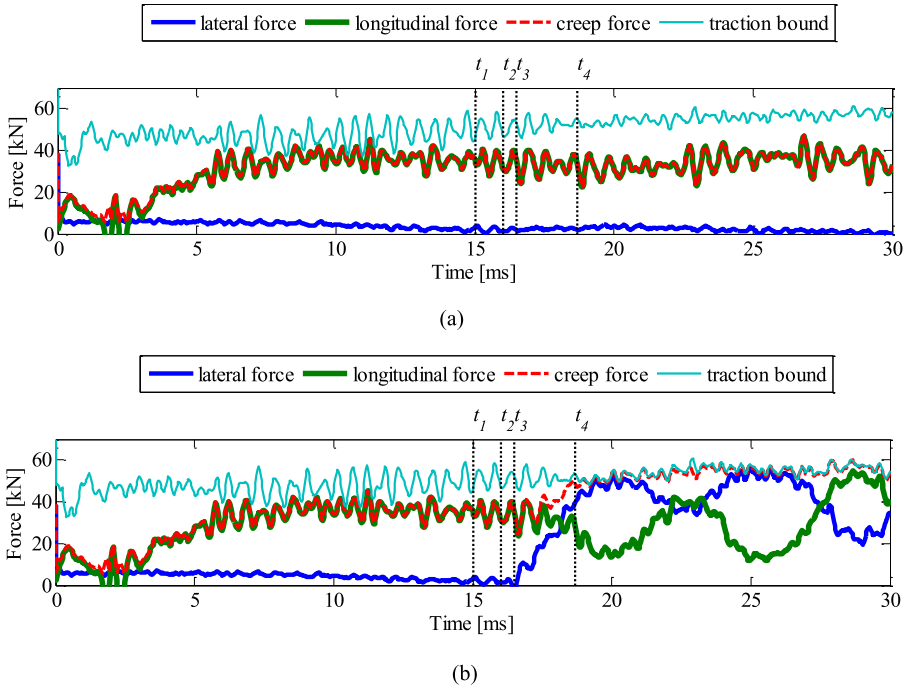


**Fig. 4.** Time histories of the simulated contact forces. (a) Contact forces simulated by case 1; (b) contact forces simulated by case 3.

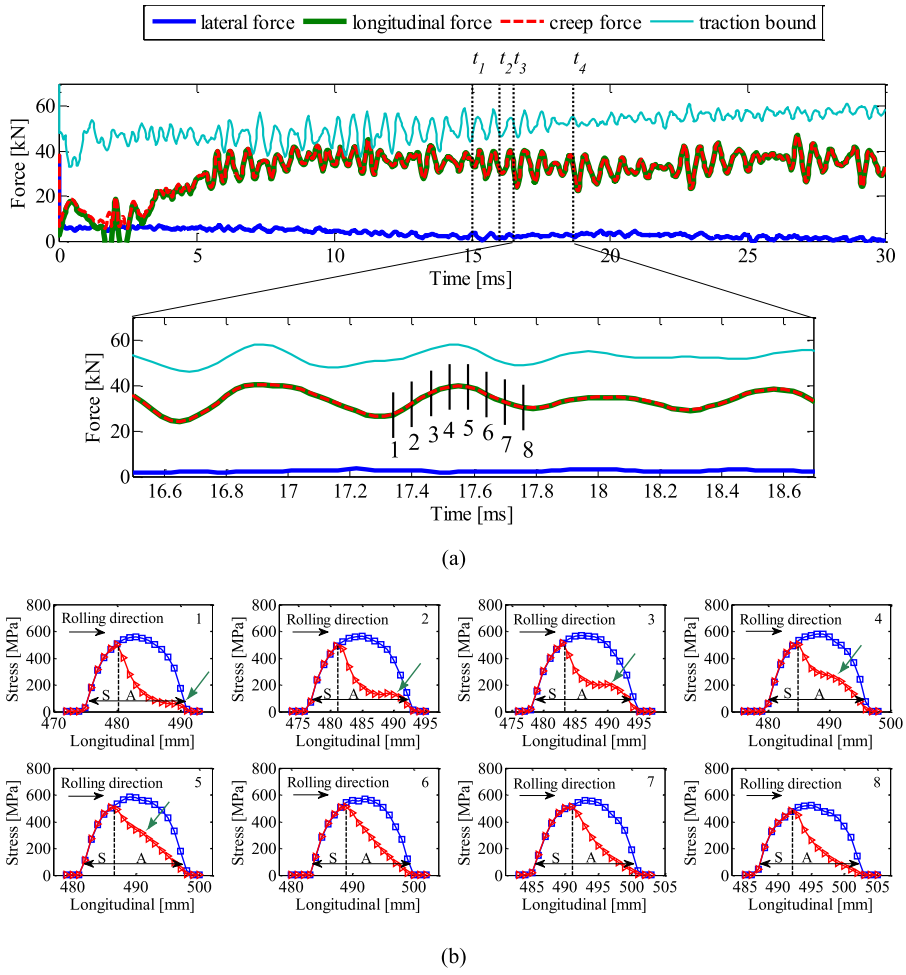


**Fig. 5.** Periodic surface stress distributions for simulation case 1. (a) Magnified view (within the solution zone) of the time histories of the contact forces for simulation case 1; (b) stress distributions calculated at corresponding time points denoted by 1–8 in (a) (blue curve: traction bound; red curve: surface shear stress; A: adhesion region; and S: slip region; the green arrows indicate the position of the moving local peak). (For interpretation of the references to color in this figure legend, the reader is referred to the web version of this article.)

'A' and 'S' in the figure, respectively. A comparison of the stress distributions calculated at the eight time points in Fig. 5(b) indicates that the surface shear stress within the adhesion region increased gradually from the 1st time point to the 4th time point and decreased from the 5th time point to the 8th time point. This trend is in accordance with the variation in the creep force shown in the magnified view of Fig. 5(a). The animation displaying the variation in the surface stress with time [34] indicates that the surface shear stress and the traction bound varied periodically with the contact forces. As reported by [10], the interface pressure distribution varies with time during vibration; thus, the periodic variation in the surface normal and shear stresses reproduced in this numerical example may reflect the dynamic effects involved in the explicit FE contact solutions.

In addition, a moving local peak of the shear stress, indicated by the green arrows in Fig. 5(b), was observed within the adhesion region in the variation process of the contact stress. The peak starts at the leading edge of the contact patch, moves towards the trailing part, and ultimately exits the adhesion region at the juncture of the adhesion-slip regions. Because the shear stress is close to the traction bound when close to the leading edge of the contact patch and when close to the juncture of the adhesion-slip regions, sudden friction saturation, or a turbulence of micro-slip [35], may arise when such a local peak of shear stress enters or exits the adhesion region.

### 3.2.2. *Contact solutions with lateral creepage*

Contact stress and micro-slip are symmetrically distributed with respect to the longitudinal axis within the contact patch when creepage exists only in the longitudinal direction. When simulating wheel lateral motion in this study, the resulting wheel-rail lateral creepage caused asymmetric distributions of contact stress and micro-slip within the contact patch, as shown in Fig. 6. To compare contact solutions with a broad range of lateral creepage, Fig. 6 plots six typical contact solutions obtained for several simulation cases: (a) and (b) were obtained with simulation case 1 at 17.58 ms and with case 2 at 17.58 ms, respectively; (c) and (e) were obtained with case 3 at 17.58 ms and 18.54 ms, respectively; and (d) and (f) were obtained with case 4 at 17.07 ms and 17.94 ms, respectively. From top to bottom, the graphs in Fig. 6 display the simulated stress distributions along the longitudinal centerline of the contact patch (1st row), stress distributions (2nd row) and micro-slip distributions (3rd row) within the contact patch, as well as shear stress and adhesion-slip region distributions obtained with Kalker's boundary element method program CONTACT [36] (4th row). The corresponding creepage values (lateral creepage $\eta$ and longitudinal creepage $\xi$) are presented in Table 3 (except for Fig. 6(f)).

Traditional rolling contact theories are generally based on the half-space assumption; the main parts of contact bodies not close to the contact point can, therefore, be considered as rigid. The creepage may then be conveniently calculated with the 'rigid' wheel-rail relative velocity and the wheel rolling velocity. However, this is no longer valid for FE contact models, which drop the half-space assumption and are flexible everywhere. The traditional method of the creepage calculation is thus not applicable for the presented explicit FE wheel-rail contact model. Considering that the explicit FEM and CONTACT should provide similar creepage-creep force relationships, as reported in [37], we estimated the corresponding creepage values of the explicit FE contact solutions using CONTACT in this study: the creep forces calculated with the

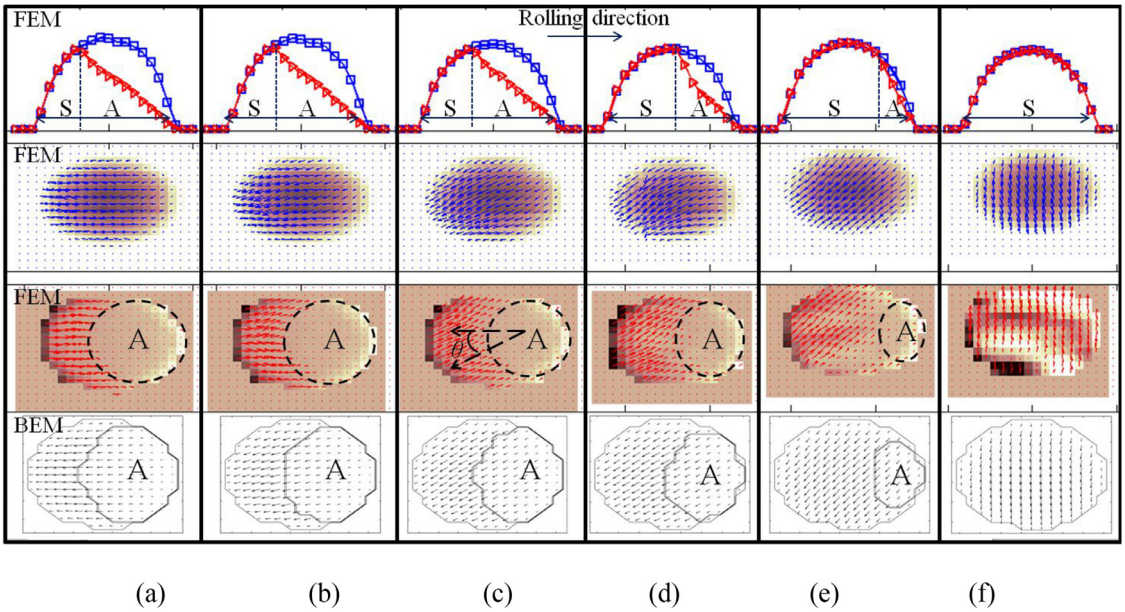


**Fig. 6.** Simulated contact solutions with lateral creepage (1st row: stress distributions along the longitudinal centerline; 2nd row: stress distributions within the contact patch (color depth: pressure magnitude; blue arrows: directions and magnitudes of the shear stress); 3rd row: micro-slip distributions (color depth: magnitude of the normal wheel-rail relative velocity; red arrows: directions and magnitudes of the micro-slips); and 4th row: shear stress and adhesion-slip region distributions calculated with Kalker's CONTACT [36] (black arrows: directions and magnitudes of the shear stress). (a) simulation case 1 at 17.58 ms; (b) case 2 at 17.58 ms; (c) case 3 at 17.58 ms; (d) case 4 at 17.07 ms; (e) case 3 at 18.54 ms; and (f) case 4 at 17.94 ms. (For interpretation of the references to color in this figure legend, the reader is referred to the web version of this article.)

**Table 3**
Input forces and output creepage in the simulations with CONTACT.

| Calculated forces and creepage corresponding to the graphs in Fig. 6 | (a) | (b) | (c) | (d) | (e) | (f) |
|---|---|---|---|---|---|---|
| Normal load $F_n$ (kN) | 126.68 | 125.61 | 123.87 | 102.60 | 116.19 | 106.46 |
| Lateral creep force $F_{ty}$ (kN) | 2.19 | 9.30 | 20.27 | 18.41 | 36.83 | 47.04 |
| Longitudinal creep force $F_{tx}$ (kN) | 39.46 | 39.19 | 38.12 | 33.59 | 34.01 | 6.09 |
| Lateral creepage $\eta$ (%) | 0.019 | 0.080 | 0.185 | 0.199 | 0.440 | – |
| Longitudinal creepage $\xi$ (%) | 0.304 | 0.308 | 0.317 | 0.331 | 0.326 | – |

explicit FE model (see Table 3) were input into the simulations with CONTACT as the prescribed tangential forces, and the other input parameters used in the CONTACT simulations were the same as those involved in the explicit FE simulations. Contact solutions and the creepage values were then obtained with CONTACT and presented in the 4th row of Fig. 6 and in Table 3, respectively. Note that no creepage value was presented for Fig. 6(f) because when friction saturation occurs, a prescribed creep force corresponds to nonunique creepage.

In the contour/vector diagrams showing the stress distributions (2nd row), the pressure magnitude corresponds to the depth of the color; the blue arrows indicate the directions of the shear stress, and their lengths are proportional to the shear stress magnitude. Similarly, in the contour/vector diagrams showing the micro-slip distributions (3rd row), the depth of the color within the contact patch indicates the magnitude of the normal wheel-rail relative velocity; the red arrows indicate the directions of the micro-slip, and their lengths are proportional to the micro-slip magnitude. The asymmetry of the distribution of the contact patch can be characterized by an orientation angle $\theta$, as shown in Fig. 6(c). The orientation angle increases with the lateral creepage from Fig. 6(a) to (e). For the solutions calculated with CONTACT (4th row), the black arrows indicate the directions of the shear stress, and their lengths are proportional to the shear stress magnitude. The orientation angles obtained with CONTACT are consistent with those obtained with the explicit FEM.

The distributions of the adhesion-slip regions determined by the simulated explicit FE contact stresses in the 1st row and the micro-slips in the 3rd row are in line with each other. They are also in reasonable agreement with the distributions of the adhesion-slip regions determined with CONTACT in the 4th row. In the graphs of the micro-slip distribution (3rd row), the slip regions covered with micro-slip vectors are located at the trailing part of the contact patch, while the adhesion regions 'A' indicated by dashed ovals shrink with increasing lateral creepage from Fig. 6(a) to (e). Fig. 6(f) shows friction saturation.

The color depth outside the contact patch corresponds to a zero normal relative velocity in the graphs of the micro-slip distribution (3rd row). Thus, the color depths at the leading and trailing edges are lighter and darker, respectively, indicating a positive and negative normal relative velocity. Wave phenomena indicated by the variation in color depth can be observed in the micro-slip distributions calculated with the explicit FEM in Fig. 6(e) and (f). Because the surface elements of the wheel and rail were in contact, further movement towards or away from each other caused transient intensification or relaxation of the contact, respectively. The waves were therefore essentially embodied in the alternation of compression intensification and relaxation [35]. According to the vibration frequencies of the rail surface nodes and the wavelengths observed in Fig. 6, the wave speed can be estimated as approximately 3 km/s, which is in line with the speed of Rayleigh wave traveling in steel. Moreover, the phase difference between normal and tangential surface nodal vibrations is approximately $\pi/2$, which also corresponds well with the Rayleigh wave.

### 3.2.3. *Contact solutions with a velocity-dependent COF*

A velocity-dependent COF defined in Eq. (7) was adopted in simulation case 5. The decay coefficient $c$, static COF $\mu_s$ and dynamic COF $\mu_d$ were set to 6, 0.5 and 0.32, respectively, as used in [29]. Fig. 7 presents one example of the contact solutions calculated with simulation case

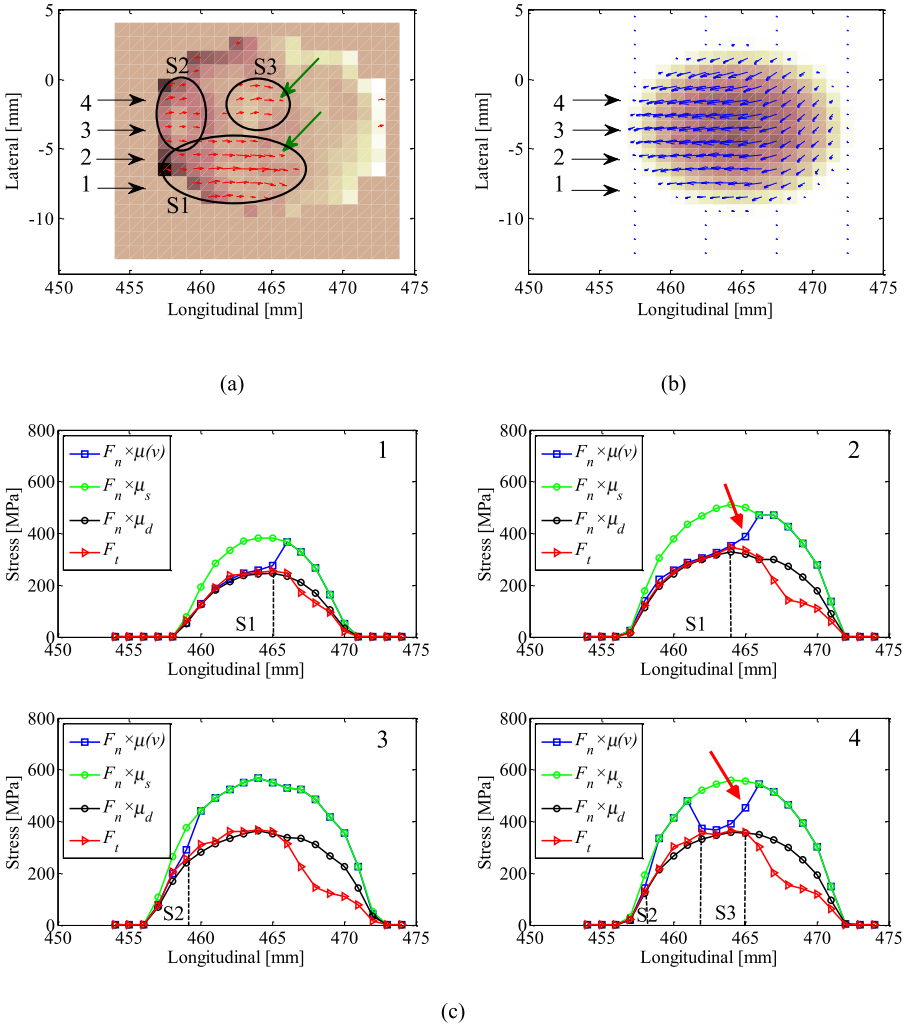


**Fig. 7.** One example of the contact solutions calculated using a velocity-dependent COF (simulation case 5. S1, S2 and S3: slip regions). (a) Adhesion-slip division determined by the micro-slip (red arrows: micro-slips); (b) stress distribution (color depth: pressure magnitude; blue arrows: directions and magnitudes of the shear stress); (c) adhesion-slip divisions determined by the stress distributions extracted from (b) along the four longitudinal lines of the contact patches indicated by black arrows. (For interpretation of the references to color in this figure legend, the reader is referred to the web version of this article.)

5 at 16.68 ms. Although simulation case 5 shared the same configuration as case 3 (except for COF), the orientation angle shown in Fig. 7(b) is much smaller than those shown in Fig. 6(c) and (e) because lateral creep force increased when the wheel passed the solution zone (see the blue curve between time $t_3$ and $t_4$ in Fig. 4(b)) and the contact solution presented in Fig. 7 was calculated at an earlier time step than those of Fig. 6(c) and (e) and thus had a smaller lateral creepage.

Fig. 7(a) shows the simulated micro-slip distribution within the contact patch. Compared to the adhesion-slip distributions simulated with a constant COF shown in Fig. 6, the adhesion-slip distribution in Fig. 7 shows a less regular pattern: the slip regions denoted by the black ovals S1, S2 and S3 are scattered in the trailing part of the contact patch. However, this result is believed to be a realistic contact condition [29].

The contact pressures and surface shear stresses plotted in Fig. 7(c) were extracted from the stress distribution shown in Fig. 7(b) along the four longitudinal lines of the contact patches indicated by black arrows. In Fig. 7(c), the red and blue curves indicate the simulated surface shear stress $F_t$ and the traction bound (the product of the contact pressure $F_n$ and the velocity-dependent COF $\mu(v)$), respectively, the green curve indicates the product of the contact pressure and the static COF $\mu_s$, and the black curve indicates the product of the contact pressure and the dynamic COF $\mu_d$.

According to Coulomb's law of statics, the blue curve in Fig. 7(c) should coincide either with the green curve of the adhesion regions or with the red curve of the slip regions. Discrepancies were, however, observed in the numerical solutions at two data points, as indicated by the two red arrows: the blue curves at these two data points should have overlapped with the red curves because the calculated micro-slips at these locations are nonzero in Fig. 7(a), as indicated by the two green arrows. These discrepancies may stem from two aspects. First, the shear stress and traction bound shown in Fig. 7(c) were obtained at different time steps. Because the velocity-dependent COF $\mu(\dot{\mathbf{u}}_{\text{rel}})$ used to calculate the traction bound (Eq. (5)) and the tangential force (Eq. (6)) at a certain time step relies on the nodal displacements obtained at the previous time step (Table 1 step (d)), the traction bound displayed in Fig. 7(c) was in fact calculated one time step later than the shear stress. Considering that the time step used in the simulation was small (approximately 86 ns), the second aspect is expected to dominate: the discrepancies were due to the different sensitivities of the approaches used to determine the slip region. The micro-slip shown in Fig. 7(a) and the velocity-dependent COF $\mu(v)$ used for Fig. 7 were calculated using the wheel-rail relative velocities, whereas the shear stress $F_t$ was obtained using the relative displacement (Eq. (4)). Because the displacement was obtained by integrating velocity (Eq. (3)) and integration can act as a filter, the traction bound shown in Fig. 7(c) is expected to reflect dynamic effects more sensitively than the surface shear stress calculated using the displacement.

The adhesion-slip distribution determined using the calculated contact stresses in Fig. 7(c) is in reasonable agreement with that determined using the calculated micro-slip in Fig. 7(a), indicating that the explicit FEM can predict wheel-rail dynamic contact solutions with velocity-dependent COFs. Because the falling-friction characteristic can be reproduced only by the velocity-dependent COF [33], the explicit FEM is expected to be capable of reproducing the falling-friction characteristic.

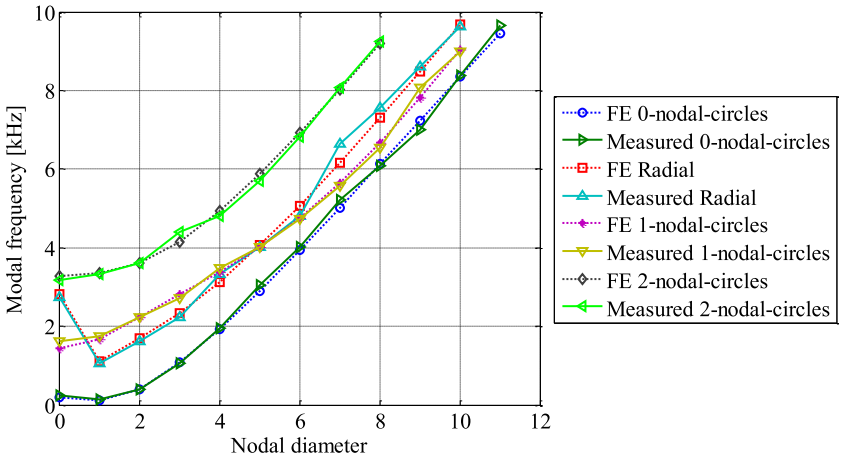


**Fig. 8.** Comparison of the calculated and measured wheel modal frequencies (solid lines: measured; dotted lines: FE simulated).

### 3.3. Wheel dynamic behavior

Based on the analysis of the simulated wheel-rail dynamic contact solution with velocity-dependent COF, the preceding subsection indicated that the explicit FEM is capable of addressing the falling-friction generation mechanism of wheel squeal. As reported in [38], an explicit FE model may include in its solution all relevant vibration modes and associated wave propagations as long as the elements and time steps are sufficiently small. The computational time step ($\Delta t$ in Eqs. (2) and (3)) of the transient analyses in this study fluctuated around 86 ns; thus, the vibration frequency up to 5.8 MHz can theoretically be predicted. This subsection analyzes the wheel dynamic behavior and compares the wheel dynamic responses simulated with and without lateral motion to address the mode-coupling mechanism of squeal.

#### 3.3.1. Validation of wheel dynamic behavior

Wheel dynamic behavior plays a more important role in the generation of high-frequency squeal than track dynamic behavior [22]. Each tonal frequency of squeal is expected to relate to a wheel mode [17, 39]. To accurately simulate wheel dynamic responses during rolling, this study first validated the dynamic behavior of the explicit FE wheel submodel with a laboratory hammer test. A typical NS-intercity wheel used in the Dutch railway was measured. Because material damping of a wheel is generally very low and the exact value of the wheel modal damping is not critical for noise prediction [22], the wheel dynamic behavior can be characterized by the modes and the corresponding natural frequencies [21, 30]. The wheel modes are generally characterized by the numbers of nodal diameters and nodal circles [22]. Fig. 8 compares the wheel vibration modes measured by the hammer test and those identified through the FE modal analysis within the frequency range of squeal (up to 10 kHz). The natural frequencies of the wheel modes in various directions are plotted against the number of nodal diameters. Measured results are plotted using solid lines and the corresponding results from the FE modal analysis are presented using dotted lines. Reasonable agreement was reached. All these physical modes were thus included in the transient dynamic simulation by virtue of the full FE model and the small time step [31].

#### 3.3.2. Squeal-like wheel vibration

After the validation of wheel dynamic behavior, wheel dynamic responses were simulated using the proposed explicit FE wheel-rail dynamic interaction model. Fig. 9(a) and (b) show the time histories and the corresponding power spectrum densities (PSDs), respectively, of the lateral vibration of the rolling wheel calculated in simulation cases 1–4. The squeal-like vibration signals represented by large amplitude limit-cycles were produced by the explicit FE model when applying the wheel lateral motion. The amplitudes of the limit cycles of the time histories

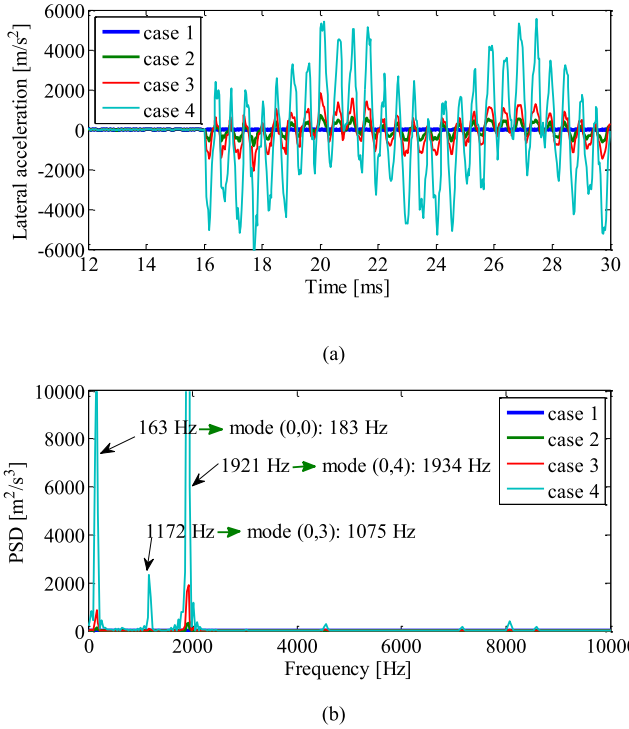


**Fig. 9.** Time histories and PSDs of the wheel lateral vibration simulated by different simulation cases. (a) Time histories; (b) PSDs.

increased with increasing amplitude of the lateral motion applied to the wheel model. The three dominant frequencies of the squeal-like vibration signals shown in PSDs in Fig. 9(b) are 163 Hz, 1172 Hz and 1921 Hz. Comparing these frequencies to the wheel modal frequencies identified in Subsection 3.3.1, we can determine the wheel modes excited in the simulations of wheel-rail dynamic interaction with wheel lateral motion: the mode with zero nodal circle and zero nodal diameter (0,0), the mode with zero nodal circle and three nodal diameters (0,3), and the mode with zero nodal circle and four nodal diameters (0,4), as shown in Fig. 9(b) and Table 4. The results correspond well to the conclusion that zero-nodal-circle modes tend to be excited in squeal [22].

#### 3.3.3. Mode-coupling behavior

Fig. 10 compares the wheel vibrations calculated with no lateral motion (case 1) and with large lateral motion (case 4). The comparison of the simulated wheel lateral vibrations in Fig. 10(a) and (d) indicates that

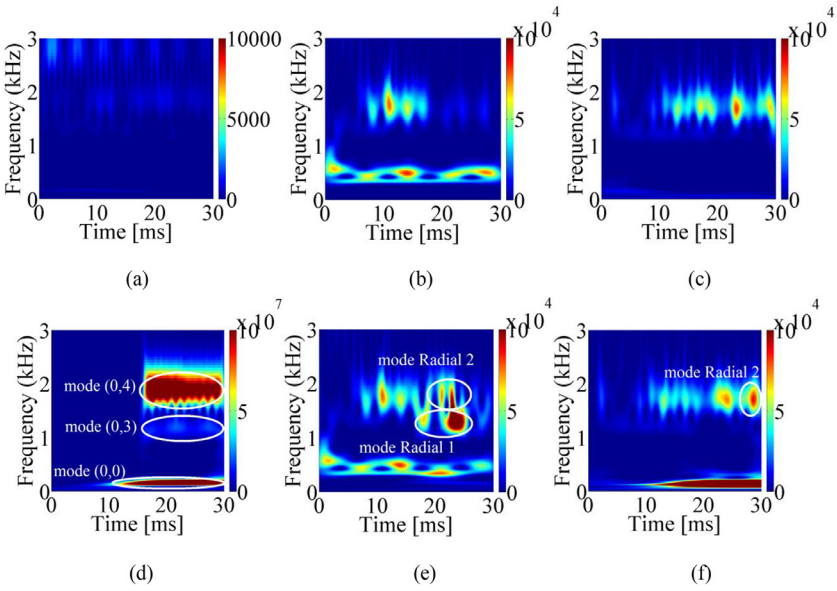


**Fig. 10.** WPSs of the simulated wheel vibration without lateral wheel motion (case 1) and with large lateral wheel motion (case 4). (a) Lateral vibration for case 1; (b) vertical vibration for case 1; (c) longitudinal vibration for case 1; (d) lateral vibration for case 4; (e) vertical vibration for case 4; (f) longitudinal vibration for case 4.

**Table 4**
Corresponding dominant frequencies of the simulated vibrations and the wheel modes.

| Dominant frequency in PSDs | Corresponding modal frequency | Corresponding mode |
|---|---|---|
| 163 Hz | 183 Hz | 0 nodal circle, 0 nodal diameter |
| 1172 Hz | 1075 Hz | 0 nodal circle, 3 nodal diameters |
| 1921 Hz | 1934 Hz | 0 nodal circle, 4 nodal diameters |

the enforcement of the lateral displacement boundary condition at time $t_2 = 16$ ms excited the out-of-plane axial modes (0,0), (0,3) and (0,4), as denoted in Fig. 10(d). The comparisons of the simulated wheel vertical and longitudinal vibrations in Fig. 10(b) and (e) and in Fig. 10(c) and (f) indicate that the prescribed wheel motion in the axle direction may also excite the in-plane radial wheel modes with one nodal diameter and two nodal diameters, which are denoted by mode Radial 1 and mode Radial 2 in Fig. 10(e) and (f), respectively. The coupling of the axial and radial dynamics shown in Fig. 10 suggests that the mode-coupling mechanism can be reproduced by the proposed explicit FE wheel-rail dynamic interaction model.

The dominant frequency component of approximately 150 Hz in Fig. 10(f) was excited mainly by the longitudinal creep force, which generally fluctuated in antiphase with the lateral creep force after time $t_3$ (see Fig. 4(b)). The dominant frequency of the creep force fluctuations can be estimated by Fig. 4(b) as approximately 150 Hz. However, because the axial wheel mode ((0,0): 183 Hz) with a close modal frequency was excited, the energy amplitude of the calculated wheel lateral vibration concentrated at approximately 150 Hz was much larger than that of the longitudinal vibration, as indicated by the color bars of Fig. 10(d) and (f).

## 4. Conclusions and future research

We have proposed an explicit FE wheel-rail dynamic interaction model with wheel lateral motion to address the falling-friction and mode-coupling mechanisms, which are commonly considered to generate squeal. The explicit FEM couples the calculation of frictional rolling contact with the calculation of structural dynamic responses and is intrinsically suitable for modeling friction-induced unstable vibration. The simulation results indicated that the proposed model can reproduce both mechanisms, thus confirming that the explicit FEM is reliable for predicting wheel-rail squeal-exciting contact and is promising for the accurate prediction of squeal.

We have analyzed the dynamic contact solutions calculated by the explicit FE wheel-rail interaction model, including contact stresses and the distributions of micro-slip and adhesion-slip regions within the contact patch. The contact solutions obtained with the explicit FE are in reasonable agreement with those obtained with Kalker's boundary element program CONTACT. Wave phenomena caused by large lateral creepage were observed in the explicit FE contact solutions. A moving local peak of shear stress was discovered within the adhesion region in the variation of contact stress, which was concluded to relate to the generation of the turbulence-induced waves reported in [35].

We also discussed the influence of the velocity-dependent COF on the dynamic contact solutions. Applying the velocity-dependent COF resulted in a less regular adhesion-slip distribution pattern, which may show a more realistic contact condition. The distributions of the adhesion-slip regions determined by the simulated contact stresses and by the micro-slips were mutually consistent when the constant COF was used, whereas small discrepancies were observed when the velocity-dependent COF was used. The discrepancies were concluded to stem from the different sensitivities of the approaches used to determine the slip region.

The dynamic behavior of the FE wheel model was validated through a laboratory hammer test. By relating the dominant frequencies of the simulated squeal-like vibration to the identified wheel modal frequencies, three zero-nodal-circle modes prone to be excited in squeal were determined and found to correspond well to previously reported results.

Because 'enigmatic' squeal is sensitive to both structural dynamic behavior and contact condition, the dynamic contact algorithms should be further studied and experimentally validated. In addition, the displacement boundary conditions applied to the proposed explicit FE wheel model may not be sufficiently accurate for simulating wheel curving behavior and rolling contact on the curve tracks. More realistic kinematic boundary conditions or a full wheelset model may be required to reliably calculate unstable wheel vibration and consequent squeal.

## Acknowledgments

This work was supported by the China Scholarship Council and the Dutch railway infrastructure manager ProRail.

## Declarations of interest

None.

Figures reproduced in color in the printed version: None.

## Supplementary materials

Supplementary material associated with this article can be found, in the online version, at doi:10.1016/j.ijmecsci.2019.02.012.

## References


[1] Pieringer A. A numerical investigation of curve squeal in the case of constant wheel/rail friction. J Sound Vibration 2014;333:4295–313. https://doi.org/10.1016/j.jsv.2014.04.024.

[2] Rudd MJ. Wheel/rail noise—Part II: Wheel squeal. J Sound Vibration 1976;46:381–94. https://doi.org/10.1016/0022-460x(76)90862-2.

[3] Remington PJ. Wheel/rail squeal and impact noise: What do we know? What don't we know? Where do we go from here? J Sound Vibration 1987;116:339–53. https://doi.org/10.1016/s0022-460x(87)81306-8.

[4] Fingberg U. A model of wheel-rail squealing noise. J Sound Vibration 1990;143:365–77. https://doi.org/10.1016/0022-460x(90)90729-j.

[5] Périard FJ. Wheel-Rail Noise Generation: Curve Squealing by Trams Doctoral thesis. Delft University of Technology; 1998.

[6] Heckl MA, Abrahams ID. Curve squeal of train wheels, Part 1: Mathematical model for its generation. J Sound Vibration 2000;229:669–93. https://doi.org/10.1006/jsvi.1999.2510.

[7] de Beer FG, Janssens MHA, Kooijman PP. Squeal noise of rail-bound vehicles influenced by lateral contact position. J Sound Vibration 2003;267:497–507. https://doi.org/10.1016/s0022-460x(03)00710-7.

[8] Huang ZY. Theoretical modelling of railway curve squeal. Doctoral thesis. University of Southampton; 2007.

[9] Graf M, Ostermeyer GP. Friction-induced vibration and dynamic friction laws: Instability at positive friction–velocity-characteristic. Tribol Int 2015;92:255–8. https://doi.org/10.1016/j.triboint.2015.06.019.

[10] Ouyang H, Nack W, Yuan Y, Chen F. Numerical analysis of automotive disc brake squeal: a review. Int J Vehicle Noise Vibration 2005;1:207. https://doi.org/10.1504/ijvnv.2005.007524.

[11] Kang J, Krousgrill CM, Sadeghi F. Analytical formulation of mode-coupling instability in disc–pad coupled system. Int J Mech Sci 2009;51:52–63. https://doi.org/10.1016/j.ijmecsci.2008.11.002.

[12] Giner-Navarro J, Martínez-Casas J, Denia FD, Baeza L. Study of railway curve squeal in the time domain using a high-frequency vehicle/track interaction model. J Sound Vibration 2018;431:177–91. https://doi.org/10.1016/j.jsv.2018.06.004.

[13] Li Z, Wang X, Zhang Q, Guan Z, Mo J, Ouyang H. Model reduction for friction-induced vibration of multi-degree-of-freedom systems and experimental validation. Int J Mech Sci 2018;145:106–19. https://doi.org/10.1016/j.ijmecsci.2018.06.039.

[14] Chiello O, Ayasse JB, Vincent N, Koch JR. Curve squeal of urban rolling stock—Part 3: Theoretical model. J Sound Vibration 2006;293:710–27. https://doi.org/10.1016/j.jsv.2005.12.010.

[15] Ding B, Squicciarini G, Thompson D, Corradi R. An assessment of mode-coupling and falling-friction mechanisms in railway curve squeal through a simplified approach. J Sound Vibration 2018;423:126–40. https://doi.org/10.1016/j.jsv.2018.02.048.

[16] Jiang J, Anderson DC, Dwight R. The Mechanisms of Curve Squeal. Noise Vibration Mitigation Rail Transport Syst 2015;126:587–94. https://doi.org/10.1007/978-3-662-44832-8_69.

[17] Vincent N, Koch JR, Chollet H, Guerder JY. Curve squeal of urban rolling stock—Part 1: State of the art and field measurements. J Sound Vibration 2006;293:691–700. https://doi.org/10.1016/j.jsv.2005.12.008.

[18] Glocker C, Cataldi-Spinola E, Leine RI. Curve squealing of trains: Measurement, modelling and simulation. J Sound Vibration 2009;324:365–86. https://doi.org/10.1016/j.jsv.2009.01.048.

[19] Zenzerovic I, Kropp W, Pieringer A. An engineering time-domain model for curve squeal: Tangential point-contact model and Green's functions approach. J Sound Vibration 2016;376:149–65. https://doi.org/10.1016/j.jsv.2016.04.037.

[20] Lai V-V, Chiello O, Brunel J-F, Dufrénoy P. Full finite element models and reduction strategies for the simulation of friction-induced vibrations of rolling contact systems. J Sound Vibration 2019;444:197–215. https://doi.org/10.1016/j.jsv.2018.12.024.

[21] Thompson DJ, Squicciarini G, Ding B, Baeza L. A state-of-the-art review of curve squeal noise: Phenomena, mechanisms, modelling and mitigation. Noise Vibration Mitigation Rail Transport Syst 2018;139:3–41. https://doi.org/10.1007/978-3-319-73411-8_1.

[22] Thompson DJ. Railway noise and vibration: Mechanisms, modelling and means of control. Elsevier; 2009.

[23] Johnson KL. Contact mechanics. Cambridge University Press; 1985.

[24] Bathe KJ. Finite element procedures. Prentice Hall; 1996.

[25] Wu SR, Gu L. Introduction to the explicit finite element method for nonlinear transient dynamics. John Wiley & Sons; 2012. Incorporated.

[26] Courant R, Friedrichs K, Lewy H. On the partial difference equations of mathematical physics. IBM J Res Dev 1967;11:215–34. https://doi.org/10.1147/rd.112.0215.

[27] Hallquist JO, Goudreau GL, Benson DJ. Sliding interfaces with contact-impact in large-scale lagrangian computations. Comput Methods Appl Mech Eng 1985;51:107–37. https://doi.org/10.1016/0045-7825(85)90030-1.

[28] Hallquist J.O. LS-DYNA Theory Manual. 2006.

[29] Zhao X, Li Z. A solution of transient rolling contact with velocity dependent friction by the explicit finite element method. Eng Comput 2016;33:1033–50. https://doi.org/10.1108/ec-09-2014-0180.

[30] Yang Z, Boogaard A, Chen R, Dollevoet R, Li Z. Numerical and experimental study of wheel-rail impact vibration and noise generated at an insulated rail joint. Int J Impact Eng 2018;113:29–39. https://doi.org/10.1016/j.ijimpeng.2017.11.008.

[31] Zhao X, Li ZL. The solution of frictional wheel-rail rolling contact with a 3D transient finite element model: Validation and error analysis. Wear 2011;271:444–52. https://doi.org/10.1016/j.wear.2010.10.007.

[32] Wei ZL, Li ZL, Qian ZW, Chen R, Dollevoet R. 3D FE modelling and validation of frictional contact with partial slip in compression-shift-rolling evolution. Int J Rail Transport 2016;4:20–36. https://doi.org/10.1080/23248378.2015.1094753.

[33] Knothe K, Wille R, Zastrau BW. Advanced contact mechanics–road and rail. Vehicle Syst. Dynamics 2001;35:361–407. https://doi.org/10.1076/vesd.35.4.361.2043.

[34] Animation for Fig. 5. https://youtu.be/3jeei3NTP84. [accessed 18.08.11].

[35] Yang Z, Li ZL, Dollevoet R. Modelling of non-steady-state transition from single-point to two-point rolling contact. Tribol Int 2016;101:152–63. https://doi.org/10.1016/j.triboint.2016.04.023.

[36] Kalker JJ. Three-dimensional elastic bodies in rolling contact. Netherlands: Springer; 1990 https://doi.org/10.1007/978-94-015-7889-9.

[37] Vo KD, Tieu AK, Zhu HT, Kosasih PB. A 3D dynamic model to investigate wheel–rail contact under high and low adhesion. Int J Mech Sci 2014;85:63–75. https://doi.org/10.1016/j.ijmecsci.2014.05.007.

[38] Zhao X, Li ZL. A three-dimensional finite element solution of frictional wheel-rail rolling contact in elasto-plasticity. Proc Inst Mech Eng Part J J Eng Tribol 2015;229:86–100. https://doi.org/10.1177/1350650114543717.

[39] Squicciarini G, Usberti S, Thompson DJ, Corradi R, Barbera A. Curve squeal in the presence of two wheel/rail contact points. Noise Vibration Mitigation Rail Transport Syst 2015;126:603–10. https://doi.org/10.1007/978-3-662-44832-8_71.